JOURNAL OF AIRCRAFT
Vol. 41, No. 5, September–October 2004

Nonlinear Flutter Aspects of the Flexible High-Speed Civil Transport Semispan Model

Muhammad R. Hajj*
Virginia Polytechnic Institute and State University, Blacksburg, Virginia 24061-0219
and
Walter A. Silva†
NASA Langley Research Center, Hampton, Virginia 23681-2199

The nonlinear aspects that lead to the flutter of the flexible semispan model of a high-speed civil transport wing configuration are analyzed. A hierarchy of spectral moments was used to determine the characteristics of the aerodynamic loading and structural strains and motions. The results show that the frequency of the bending motion of the wing varied significantly as the Mach number was increased between 0.90 and 0.97. Examination of the pressure coefficients in terms of mean value and fluctuations showed that the flow characteristics over the wing changed significantly around a Mach number of 0.97. A strong shock was identified near the trailing edge. Nonlinear analysis of the pressure fluctuations, under these conditions, showed nonlinear coupling involving low-frequency components at pressure locations where the mean value was at a local minimum. This shows that the aerodynamic forces acting on the model had nonlinearly coupled frequency components. The presented results show how nonlinear analysis tools can be used to identify nonlinear aspects of the flutter phenomenon, which are needed in the validation of nonlinear computational methodologies.

Introduction

FLUTTER instabilities encountered in flight into or through the transonic regime can cause significant motions, damage, or loss of the aircraft. Because of the complexities involved in the aerodynamic and structural aspects of the flutter phenomenon, the prediction of its boundaries is extremely difficult. Predictions based on linear models do not take into consideration complex aspects such as flow separation, shock formation, large structural deformations, or nonlinear coupling between the fluid flow and the structural motions. On the other hand, any methodology proposed for modeling nonlinear aerodynamic and structural aspects of flutter phenomena needs to be validated. Considering the current limitations of computing power and technologies, one has to assess the viability of using inviscid or viscous codes with different turbulence models, the number of degrees of freedom, and the forms of the structural operators.

The aforementioned issues point to the need for identification of nonlinear aspects of flutter. Such identification can be used as a benchmark for validation of nonlinear computational codes and methodologies against experimental data. Additionally, it would allow for determination of optimal measurements for prediction of onset of aeroelastic instabilities, assist in the development of reduced-order models, and provide effective means for obtaining improved performance with reduced uncertainties through operation beyond boundaries based on linear analysis.

The goal of this effort is to identify nonlinear aspects that lead to the flutter of a high-speed civil transport (HSCT) flexible semispan model (FSM) in experiments conducted at the NASA Langley Research Center. The high-amplitude responses observed in these experiments in different regions and with different characteristics present a unique opportunity for determining nonlinear aspects of the flutter mechanism of this configuration. Of particular interest for this work is a high-dynamic-response region that occurred over a large range of dynamic pressures around a Mach number of 0.98. At the top of this region is a "hard" flutter point that resulted in the loss of the model. The characteristics of the aerodynamic loading and structural strains and motions, as the hard flutter is encountered, are determined through analysis of pressure, strain, and acceleration data. The nonlinear aspects are identified by using higher-order spectral moments. The use of these moments to investigate limit-cycle responses observed on fighter aircraft was also proposed by Stearman et al.[1]

Experimental Setup

The FSM experiments were conducted in the Transonic Dynamics Tunnel (TDT) at NASA Langley Research Center. The TDT is a closed-circuit, continuous-flow, variable-pressure, wind tunnel with a 16-ft square test section with cropped corners. The tunnel uses either air or a heavy gas as the test medium, can operate at stagnation pressures from near vacuum to atmospheric, has a Mach number range from near zero to 1.2, and is capable of maximum Reynolds numbers of about 3 million per foot in air and 10 million per foot in heavy gas. The tests, analyzed here, were conducted in the spring of 1996 with dichlorodifluoromethane (R-12) as the test medium. Since 1998, 1,1,1,2-tetrafluoroethane (R-134a) has been used as the test medium instead of R-12. The TDT is specially configured for flutter testing, with excellent model visibility from the control room and a rapid tunnel shutdown capability for model safety (bypass valves).

The model planform[2] was a one-twelfth scale configuration based on an early design known as the Reference H configuration. To accommodate pressure instrumentation at the wing tip of the model, the original Reference H airfoil thickness was increased to a constant 4% thickness over the entire wing span. Figure 1 shows the planform layout and main components of the model. The leading and trailing edges were removable to access pressure instrumentation in those regions. A removable tip cap allowed access to pressure instrumentation at the wing tip. It should be noted that the FSM was not intended to be a flutter clearance model but, rather, a model that would exhibit an HSCT-like flutter mechanism within the range

Presented as Paper 2003-1515 at the AIAA/ASME/ASCE/AHS/ASC 44th Structures, Structural Dynamics, and Materials Conference and Exhibit, Norfolk, VA, 7–10 April 2003; received 2 May 2003; revision received 12 December 2003; accepted for publication 17 December 2003.

*Professor, Department of Engineering Science and Mechanics, 0219 Norris Hall; mhajj@vt.edu.

†Senior Research Scientist and Senior Aerospace Engineer, Aeroelasticity Branch, Structures and Materials Competency. Associate Fellow AIAA.

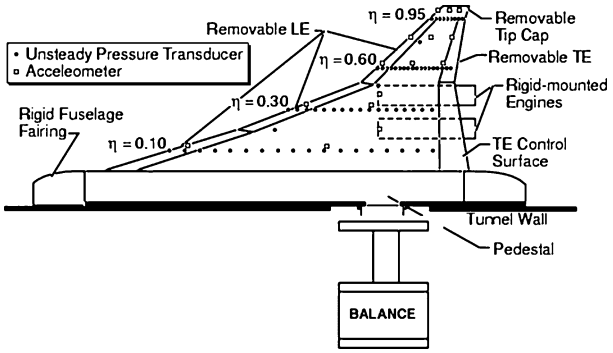

Fig. 1 Planform and instrumentation layout for the FSM wind-tunnel model.

of operation of the TDT. As such, and to induce flutter at around 200 psf, a 2.2-lb mass was added to the aft tip section. This mass was fabricated out of tungsten and bonded into the outboard removable trailing-edge section of the FSM (see Fig. 1). Additional reinforcements and local strengthening of the attachment surface between the main wing box and the outboard removable trailing-edge section were performed to handle the added stress of the additional mass.

The instrumentation layout consisted of 131 in situ unsteady pressure transducers located at the 10, 30, 60, and 95% span stations (Fig. 1). Six additional unsteady pressure transducers were installed at the 20% chord station for the 20, 45, and 75% span stations for both upper and lower surfaces. Channels were carved into the foam core to accommodate the wiring for the instrumentation. Specially designed pressure transducer holders were used to eliminate any leakage around the transducer and to provide easy access to the transducers. Instrumentation also included 14 accelerometers installed throughout the wing (Fig. 1). The FSM was instrumented with three bending strain gauges and one torsion strain gauge. All gauges were located at midspan, a region of high stress concentrations. One bending strain gauge was placed near the leading edge and will be referred to as the forward strain gauge or FWD. Another was placed near the trailing edge and will be referred to as the aft strain gauge or AFT. The third was placed at midchord and will be referred to as the middle strain gauge or MID. The torsion strain gauge was placed at midchord.

Data Analysis

The aerodynamic and structural aspects of the flutter phenomenon are determined via a frequency domain analysis that is based on a hierarchy of spectral moments. The power spectrum is used to determine the distribution of power among the frequency components in the pressure, strain, and acceleration data. The cross-power spectrum, its normalized value, the linear coherence, and the phase relation of the same frequency components between different signals are used to characterize the bending and torsion characteristics of the model. The nonlinear aspects of the aerodynamic loading are determined from estimates of higher-order spectral moments, namely, the auto- and cross-bispectrum. For a discrete, stationary, real-valued, zero-mean process, the autobispectrum is estimated as[3]

$$\hat{B}_{xxx}[l_1, l_2] = \frac{1}{M}\sum_{k=1}^{M}\left|X_T^{(k)}[l_1+l_2]X_T^{*(k)}[l_1]X_T^{*(k)}[l_2]\right|^2 \quad (1)$$

where $X_T^{(k)}[l]$ is the discrete Fourier transform of the kth ensemble of the time series $x(t)$ taken over a time T and M is the number of these ensembles. The autobispectrum of a signal is a two-dimensional function of frequency and is generally complex valued. In averaging over many ensembles, the magnitude of the autobispectrum will be determined by the presence of a phase relationship among sets of the frequency components at l_1, l_2, and l_1+l_2. If there is a random phase relationship among these three components, the autobispectrum will average to a very small value. Should there be a phase relationship among these frequency components, the corresponding autobispectrum will have a large magnitude.[4] Because a quadratic nonlinear interaction between two frequency components l_1 and l_2 yields a phase relation between them and their sum component l_1+l_2, the autobispectrum can be used as a measure that detects quadratic coupling or interaction among different frequency components of a signal. The level of such coupling in a signal can then be associated with a normalized quantity of the autobispectrum, called the autobicoherence, defined as

$$b^2_{xxx}[l_1, l_2] = \frac{(1/M)\sum_{k=1}^{M}\left|X_T^{(k)}[l_1+l_2]X_T^{*(k)}[l_1]X_T^{*(k)}[l_2]\right|^2}{(1/M)\sum_{k=1}^{M}\left|X_T^{(k)}[l_1]X_T^{(k)}[l_2]\right|^2 (1/M)\sum_{k=1}^{M}\left|X_T^{(k)}[l_1+l_2]\right|^2} \quad (2)$$

By Schwarz inequality, the value of $b^2_{xxx}[l_1, l_2]$ varies between zero and one. If there is no phase relationship among the frequency components at l_1, l_2, and l_1+l_2, the value of the autobicoherence will be near zero. If there is a phase relationship among the frequency components at l_1, l_2, and l_1+l_2, then the value of the autobicoherence will be near unity. Values of the autobicoherence between zero and one indicate partial quadratic coupling.

For systems where multiple signals are considered, detection of nonlinearities can be achieved by using the cross-spectral moments. For two signals $x(t)$ and $y(t)$, their cross-bispectral density function is estimated as

$$\hat{B}_{yxx}[l_1, l_2] = \frac{1}{M}\sum_{k=1}^{M}\left|Y_T^{(k)}[l_1+l_2]X_T^{*(k)}[l_1]X_T^{*(k)}[l_2]\right|^2 \quad (3)$$

where $X_T^{(k)}[l]$ and $Y_T^{(k)}[l]$ are the discrete Fourier transforms of the kth ensemble of the time series $x(t)$ and $y(t)$, respectively, and are taken over a time T. The cross-bispectrum, as defined in Eq. (3), provides a measure of the nonlinear relation among frequency components at l_1 and l_2 in $x(t)$ and their sum frequency component l_1+l_2 in $y(t)$. Similar to the autobispectrum, the cross-bispectrum of signals $x(t)$ and $y(t)$ is a two-dimensional function in frequency and is generally complex valued. In averaging over many ensembles, the magnitude of the cross-bispectrum will also be determined by the presence of a phase relationship among sets of the frequency components at l_1, l_2, and l_1+l_2. If there is a random phase relationship among the three components, the cross-bispectrum will average to a very small value. Should there be any phase relationship among these frequency components, the corresponding cross-bispectral value will have a large magnitude. The cross-bispectrum is then able to detect nonlinear phase coupling among different frequency components in two signals because of its phase-preserving effect.

Similarly to defining the autobicoherence, one can define a normalized cross-bispectrum to quantify the level of quadratic coupling in two signals. This normalized value is called the cross-bicoherence and is defined as follows:

$$b^2_{yxx}[l_1, l_2] = \frac{(1/M)\sum_{k=1}^{M}\left|Y_T^{(k)}[l_1+l_2]X_T^{*(k)}[l_1]X_T^{*(k)}[l_2]\right|^2}{(1/M)\sum_{k=1}^{M}\left|X_T^{(k)}[l_1]X_T^{(k)}[l_2]\right|^2 (1/M)\sum_{k=1}^{M}\left|Y_T^{(k)}[l_1+l_2]\right|^2} \quad (4)$$

If there is no phase relationship among frequency components at l_1, l_2 in $x(t)$ and the frequency component at l_1+l_2 in $y(t)$, the value of the cross-bicoherence will be near zero. If there is a phase relationship among these frequency components, the value of the cross-bicoherence will be near unity. Values of cross-bicoherence between zero and one indicate partial quadratic coupling. A digital procedure for computing the auto- and cross-bicoherence is given by Kim and Powers[3] and is summarized by Hajj et al.[5]

Results and Discussion

Response Regions of the Flexible Semispan Model

A plot summarizing the dynamic responses that were encountered during flutter testing of the FSM is shown in Fig. 2. Silva et al.[2] provide a detailed discussion of the different regions in this plot. Of particular interest in this figure is the narrow "chimney" region of high dynamic response that spans over a Mach number range from about 0.98 to 1.0 and a deep dynamic pressure range that starts at about 160 psf. At a dynamic pressure of about 250 psf, hard flutter took place, which resulted in the loss of the model. In the next sections, we present variations observed in strain, acceleration, and pressure measurements as the flutter boundary is approached and the hard flutter point is encountered. The run number, Mach number, and dynamic pressure at these points are given in Table 1.

Motion Characterization with Strain Gauges

Measurements from the three bending strain gauges and the torsion gauge are used to characterize the response of the FSM. Figure 3 shows the spectra of the torsion and middle bending strain gauges under the test conditions of Table 1. In all results, the torsion strain gauge shows a peak near 12.7 Hz. The peak in the middle bending strain gauge decreases continuously between runs 1062 and runs 1066. In run 1067, the peak in the middle bending strain gauge is near a value of 12.7 Hz. These results show that the 12.7-Hz frequency is associated with a torsion mode and remains the same in all runs. The bending frequency, however, varies continuously.

The power spectra of the three bending strain gauges at the test conditions presented in Table 1 are shown in Fig. 4. In run 1062, each of the power spectra of the three gauges shows a significant peak near 12.7 Hz, the peak in the torsion motion. The forward gauge shows a peak near 17 Hz. For the conditions of runs 1063 and 1064, the spectra of all three bending gauges have peaks at 7.8 Hz. The power level of the peak in the forward gauge is significantly larger than the ones in the middle and aft gauges. Moreover, all spectra show relatively smaller peaks at 12.7 Hz. The spectra of run 1065 show peaks at 5.8 and 7.3 Hz in addition to a smaller peak at 12.7 Hz. Again, the power level in the forward gauge is much larger than the levels in the middle and aft gauges. In run 1066, the highest peak in the forward gauge is at 14.6 Hz with significant peaks at 12.7 and 5.4 Hz. On the other hand, the highest peak in middle and aft gauges is at 12.2 Hz with significant peaks at 5.4 and 12.7 Hz. As flutter is approached, in run 1067, the spectra of the forward gauge has one significant peak near 14.2 Hz with a relatively smaller one at 12.7 Hz. The peak in the spectra of the middle and aft gauges is at 12.7 Hz. Additionally, one difference must be stressed. The spectra in run 1067 show significantly higher levels at the lowest measured frequency, 0.5 Hz.

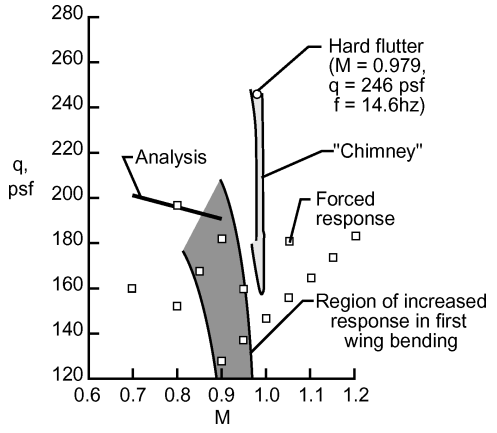

Fig. 2 Summary of the flutter and high-dynamic-response regions for the FSM wind-tunnel model.[2]

Table 1 Run numbers and test conditions

Run	Mach number	Dynamic pressure, psf
1062	0.922	226.58
1063	0.933	230.23
1064	0.940	232.83
1065	0.950	236.00
1066	0.962	240.11
1067	0.967	239.66
Model lost	0.979	245.80

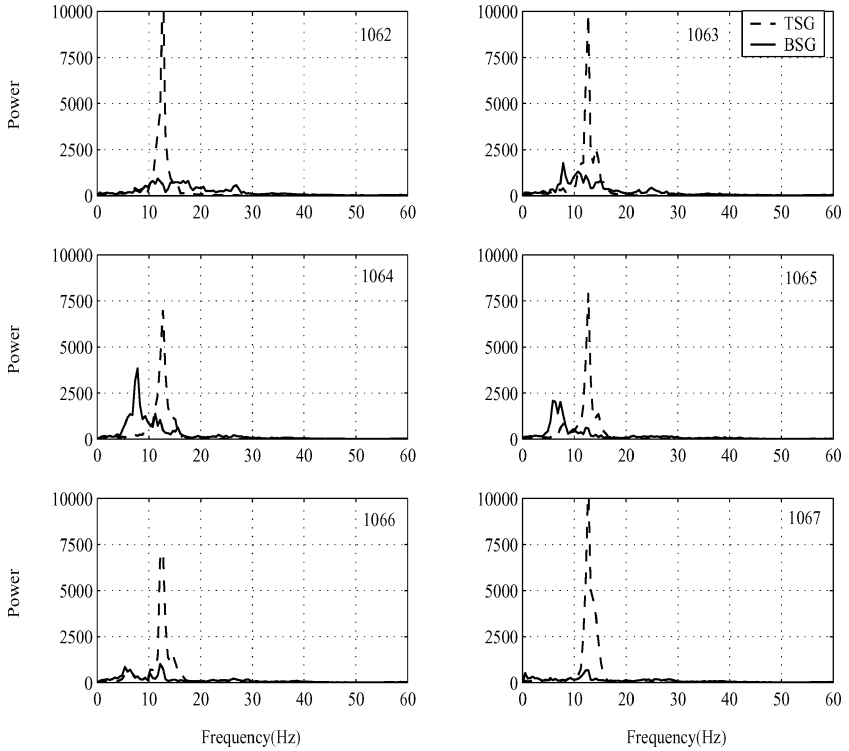

Fig. 3 Power spectra of the torsion and middle bending strain gauges.

In summary, the analysis of the response of the strain gauges shows a frequency around 12.7 Hz, which is associated with a torsion mode. The bending frequency decreased as the Mach number was increased between 0.9 and 0.96. Around a Mach number of 0.97, however, this frequency increased. As will be discussed later, this variation in the frequency is mostly due to changing flow characteristics.

To aid in the analysis of the results obtained with the power spectrum, cross-power spectra between the three gauges were obtained. The level of coherence along with the phase difference between peak frequency components are shown in Table 2. The results clearly show that the low-frequency peaks are highly coherent in all runs with near zero phase difference. This indicates that these peaks represent a bending motion. As for the 12.7 Hz, which is present in all spectra, the results show an improved level of coherence as flutter is approached. Additionally, the results show a phase difference between the three gauges, which agrees with the argument that the 12.7 Hz represents a torsional motion which becomes highly coherent as flutter is approached. As for the 14.2 Hz peak that appears in the forward strain gauge in run 1067, the results show a high level of coherence with the other gauges with a phase difference. Examining the mode shapes of the wing shows that this mode is close to one of the wind-off modes of the FSM.

Table 2 Phase difference and coherence between strain gauge peaks

		Phase difference, rad		Coherence	
Run	Peaks, Hz	FWD-MID	MID-AFT	FWD-MID	MID-AFT
1062	12.7	2.00	0.34	0.25	0.75
	15.0	0.13	0.49	0.90	0.74
	17.5	−0.15	−0.12	0.97	0.88
1063	7.8	−0.03	0.03	0.98	0.97
	10.2	0.02	0.12	0.92	0.93
	12.7	1.28	0.64	0.55	0.78
1064	7.8	−0.003	0.06	0.99	0.98
	12.7	1.43	2.77	0.06	0.43
1065	5.8	0.02	0.09	0.99	0.96
	7.3	−0.02	0.02	0.98	0.94
	12.7	1.38	2.34	0.68	0.67
1066	5.4	0.07	0.16	0.98	0.94
	12.7	1.67	2.16	0.80	0.84
	14.6	0.62	2.37	0.81	0.73
1067	12.7	2.26	2.60	0.89	0.94
	14.2	0.67	2.52	0.93	0.93

Motion Characterization with Accelerometers

Spectra of the accelerations of the wing tip are shown in Fig. 5. The results show that the wing-tip accelerations in the middle and near the leading and trailing edges have a peak of about 12.7 Hz. Moreover, there is no indication of the decrease in the frequency of the wing bending observed in the spectra of the strain gauges. It should also be noted that the spectra of the accelerations do not show distinctive effects that identify any variations as the flutter boundary is crossed.

Surface Loads and Aerodynamic Characterization with Pressure Transducers

Mean values of the pressure coefficients C_p at the 95 and 60% span stations along the chord on both upper and lower surfaces of the wing are shown in Fig. 6. The results show a small decrease in the pressure coefficient at different chord locations as the Mach number is increased. This is especially true on the upper surface. Moreover, at specific locations, such as $x/c = 30$ and 80% along the 95% span and $x/c = 55$ and 85% along the 60% span, there is a local increase, in the absolute sense, in the pressure coefficient along the chord. This increase could result from different flow effects, one of which is the formation of shocks on the surface of the wing. In particular, we note the large increase in mean pressure around the 80% chord location on both surfaces in run 1067. This large increase in pressure is most likely due to the formation of a strong shock near the trailing edge.

Figure 7 shows the power spectra of the pressure fluctuations at specified chord locations on the upper surface along the 60% span. These locations were chosen because they either have a low mean pressure coefficient or they are near the trailing edge in the region after the shock. Of interest in this figure is the significant change in the characteristics of the pressure fluctuations at the different locations. The fluctuations of amplitudes in runs 1062, 1063, and 1064 are the largest at the chord location $x/c = 80\%$. The peak amplitudes are at frequencies corresponding to those measured by the bending strain gauges. In runs 1065 and 1066, the level of the pressure fluctuations

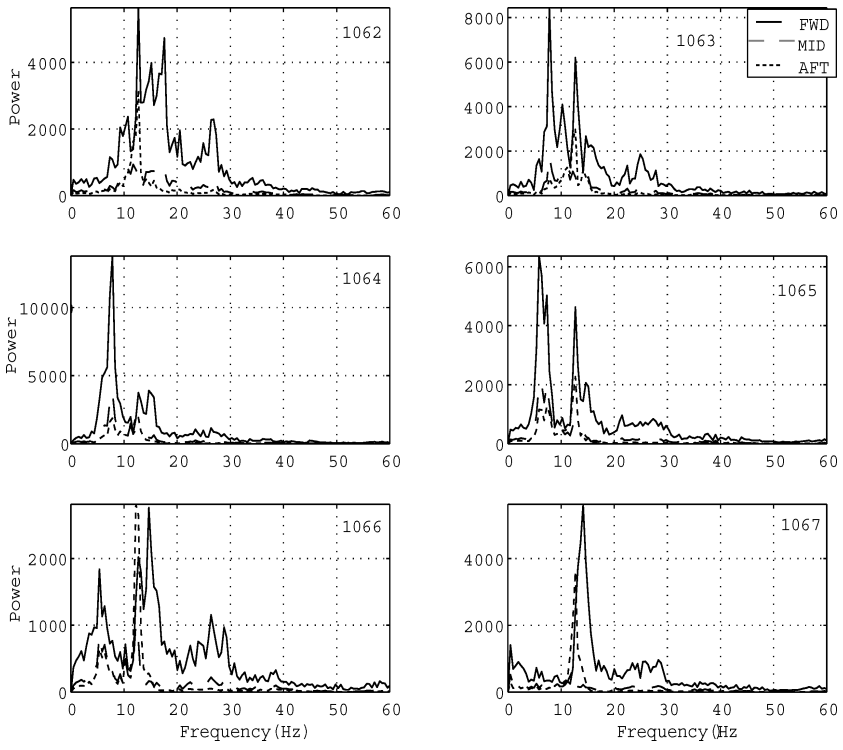

Fig. 4 Power spectra of the forward, middle, and aft bending strain gauges.

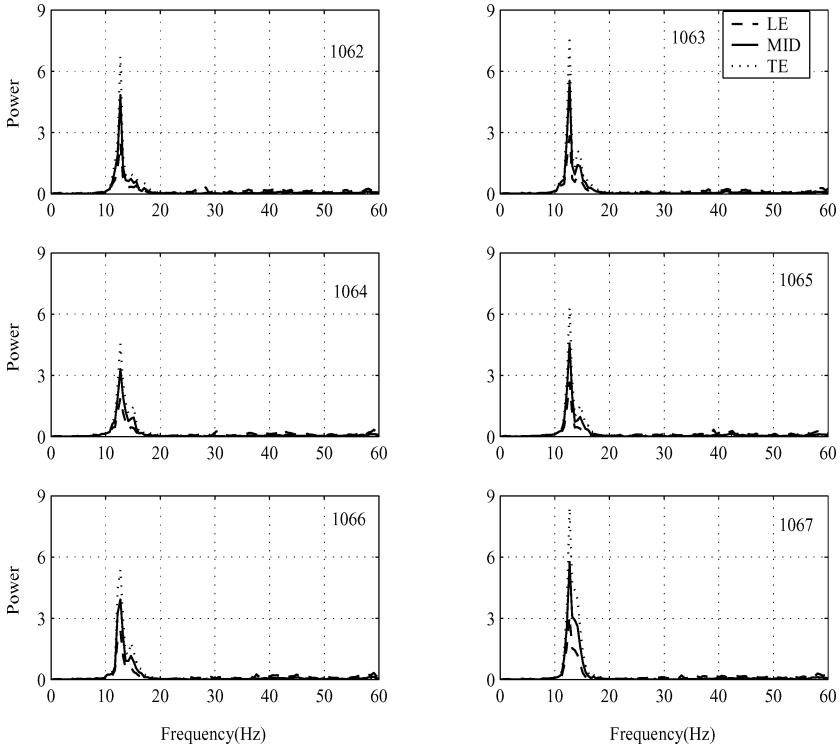

Fig. 5 Power spectra of the leading-, middle, and trailing-edge accelerometers.

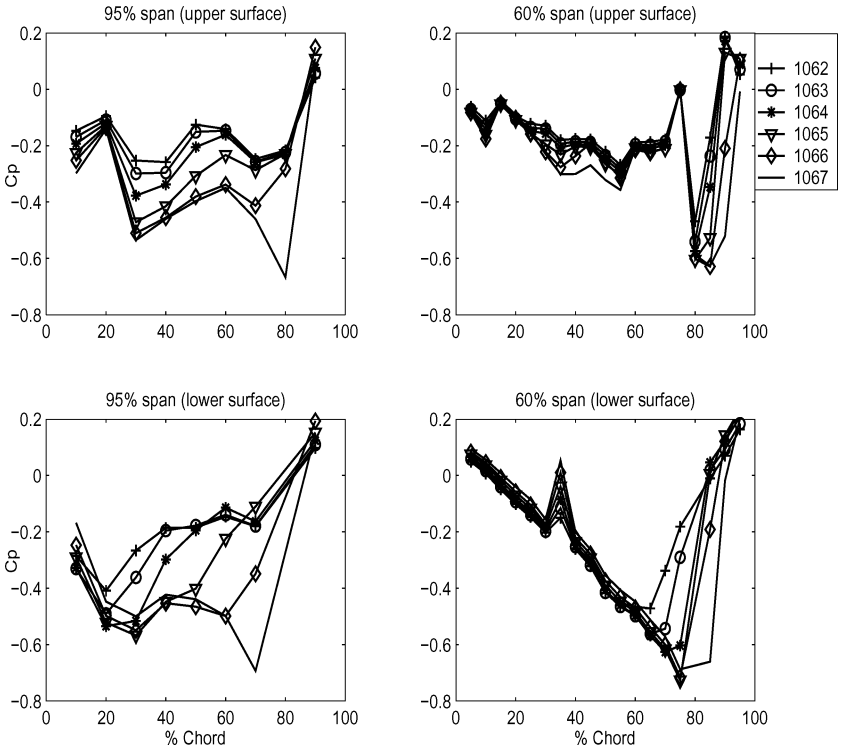

Fig. 6 Mean C_p at 60 and 95% span locations.

decreased with larger amplitudes at the chord location $x/c = 95\%$. The frequencies of the peaks still corresponded with those observed in the bending strain gauge measurements. As for run 1067, the largest peaks are observed over a band of low frequencies that do not correspond to any peaks observed in the spectra of the strain gauges. This clearly indicates a change in the flow character in run 1067 when compared to the other runs. This change is due to the formation of the shock which could be deduced from Fig. 6. Spectra at similar locations along the 95% span are shown in Fig. 8. As in the spectra along the 60% span, the results show a shift in the peaks from frequency components that match peaks observed in the strain gauge spectra in all runs except for run 1067. Additionally, the peaks in run 1067 at the chord location $x/c = 90\%$ match with those observed at $x/c = 95\%$ at the 60% chord location. This shows that the aerodynamic phenomenon causing this peak extends over a wide range of the model.

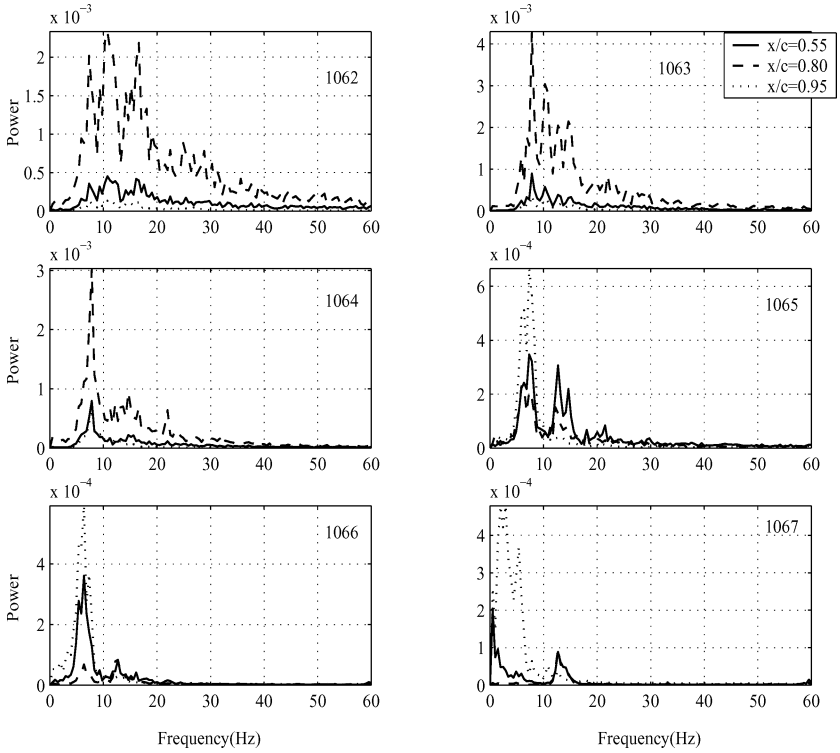

Fig. 7 Power spectra of the pressure fluctuations along 60% span at specified chord locations on the upper surface.

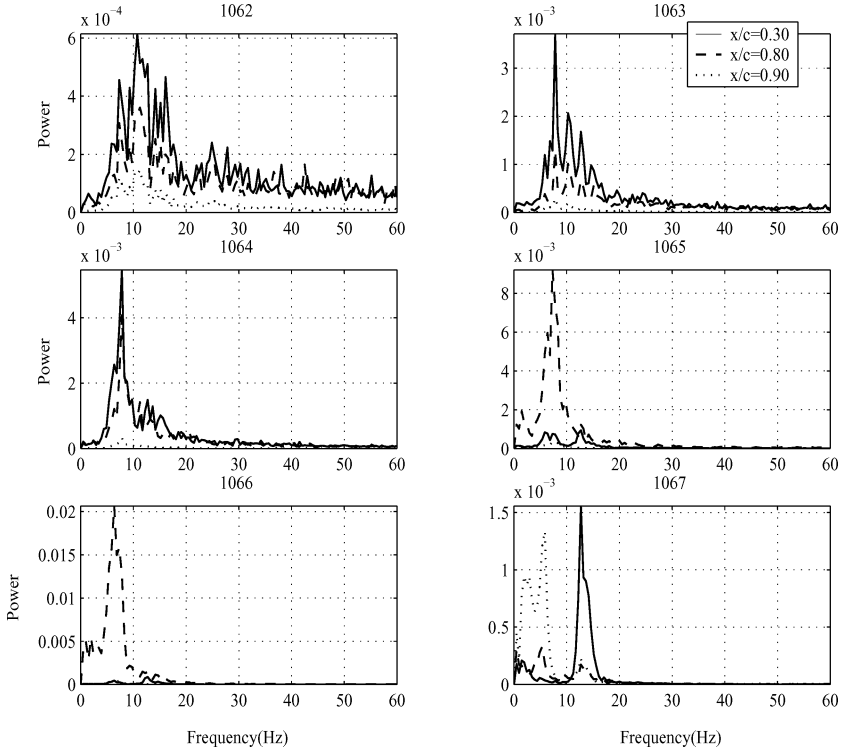

Fig. 8 Power spectra of the pressure fluctuations along 95% span at specified chord locations on the upper surface.

Further insight into the origin and role of the low-frequency components observed in the pressure spectra of run 1067 can be obtained from the autobispectra of the pressure fluctuations on the upper surface at $x/c = 0.55$ at the 60% span and at $x/c = 0.80$ at the 95% span, which are shown in Fig. 9. At $x/c = 0.80$, the results show a high level of nonlinear coupling between 0.5 Hz and the region between 3.0 and 11.0 Hz. This nonlinear coupling has its origin in the flowfield and implies that flow structures with these frequencies are coupled. On the other hand, there is no notion of coupling between the 0.5-Hz component and the frequency components observed in the strain gauge measurements, namely 12.7 and 14.2 Hz. This indicates that the detected nonlinear effects in the pressure data at these locations are aerodynamic in nature. The autobispectrum at $x/c = 0.55$ at the 60% span station shows self-coupling at 0.5 Hz. Estimates of the autobispectrum at other pressure taps did not show nonlinear coupling at the same levels observed in these taps. Yet it is important to note that these taps are at locations where the pressure coefficients are relatively large in the absolute sense.

The extent of nonlinear coupling between frequency components at both pressure taps is determined with the cross-bicoherence,

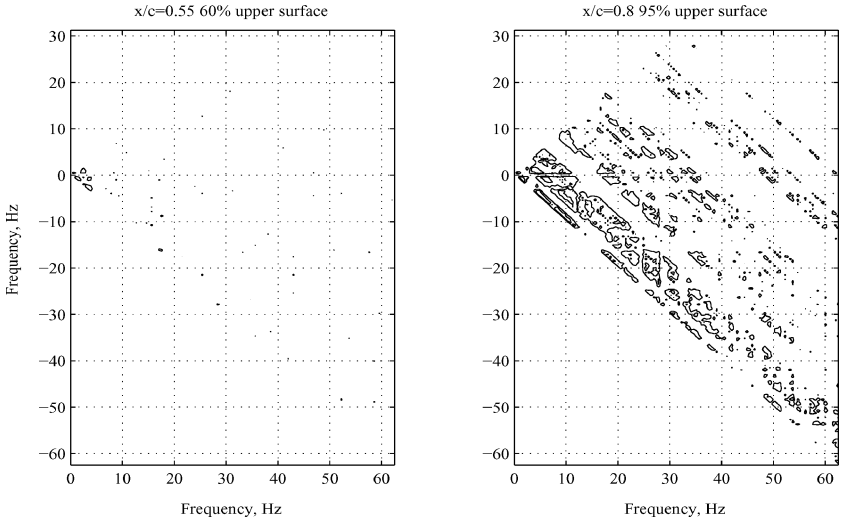

Fig. 9 Autobicoherence of the pressure fluctuations at specified chord locations on the upper surface; contour levels are set at 0.4 and 0.7.

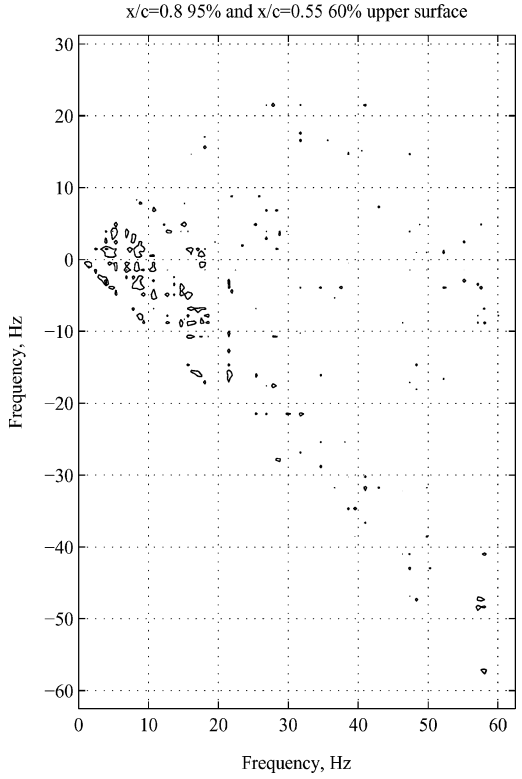

Fig. 10 Cross-bicoherence of the pressure fluctuations at specified chord locations on the upper surface; contour levels are set at 0.4 and 0.7.

which is shown in Fig. 10. The results show that the 0.5-Hz component at $x/c = 0.55$ at the 60% span station is coupled with several components at $x/c = 0.80$ at the 95% span station. This shows that pressure forces acting at these locations contain nonlinearly coupled frequency components. The importance of these results lies in the fact that this nonlinearity, involving the low-frequency components, was only observed in run 1067 as the flutter point is approached and is associated with the formation of the shock. Moreover, this gives insight into the origin of the low-frequency component observed in the strain gauges in run 1067 (see Fig. 4).

Conclusions

In this work, flutter aspects that lead to the structural failure of an HSCT FSM were analyzed. Spectral analysis was used to determine the characteristics of the aerodynamic loading and structural strains and motions. In particular, higher order spectral moments, namely the auto- and cross-bispectrum, were used to identify nonlinear aspects of this flutter phenomenon. The results show important and new insights. The frequency of the bending motion of the wing decreased continuously as the Mach number was increased between 0.90 and 0.96. Around a Mach number of 0.97, this frequency increased. Examination of the pressure coefficients in terms of mean value and fluctuations showed that the flow characteristics over the wing changed significantly around a Mach number of 0.97. A strong shock was identified near the trailing edge. Nonlinear analysis of the pressure fluctuations, under these conditions, showed nonlinear coupling involving low-frequency components at pressure taps where the mean value was at a local minimum. This indicates that the aerodynamic forces acting on the model had nonlinearly coupled frequency components. These results show how nonlinear analysis tools can be used to provide insights into nonlinear flutter, which is needed in the validation of nonlinear computational methodologies.

Acknowledgments

This work was also partially supported by AFOSR under Grant F49620-03-1-0206. The assistance of the Office of Education at NASA Langley Research Center through the NASA Faculty Fellowship Program is greatly appreciated. The first author would like to also thank all personnel of the Aeroelasticity Branch for their hospitality during the summer of 2002.

References

[1]Stearman, R. O., Powers, E. J., Schwartz, J., and Yurkovich, R., "Aeroelastic System Identification of Advanced Technology Aircraft Through Higher Order Signal Processing," *Proceedings of the 9th International Modal Analysis Conference*, Vol. 2, Society of Experimental Mechanics, Bethel, CT, 1992, pp. 1607–1610.

[2]Silva, W. A., Keller, D. F., Florance, J. R., Cole, S. R., and Scott, R. C., "Experimental Steady and Unsteady Aerodynamic and Flutter Results for HSCT Semispan Models," AIAA Paper 2000-1697, April 2000.

[3]Kim, Y. C., and Powers, E. J., "Digital Bispectral Analysis and Its Applications to Nonlinear Wave Interactions," *IEEE Transactions on Plasma Science*, Vol. PS-7, No. 2, 1979, pp. 120–131.

[4]Hajj, M. R., Miksad, R. W., and Powers, E. J., "Fundamental-Subharmonic Interaction: Effect of the Phase Relation," *Journal of Fluid Mechanics*, Vol. 256, 1993, pp. 403–426.

[5]Hajj, M. R., Miksad, R. W., and Powers, E. J., "Perspective: Measurements and Analyses of Nonlinear Wave Interactions with Higher-Order Spectral Moments," *Journal of Fluid Engineering*, Vol. 119, No. 3, 1997, pp. 3–13.